applied optics

Intensity distribution of the parhelic circle and embedded parhelia at zero solar elevation: theory and experiments

Sarah Borchardt[1] and Markus Selmke[2,*]

[1]Universität Leipzig, Linnéstr. 5, 04103 Leipzig, Germany
[2]Department of Chemistry, Princeton University, Princeton, New Jersey 08544, USA
*Corresponding author: markus.selmke@gmx.de

Received 4 May 2015; revised 18 June 2015; accepted 29 June 2015; posted 29 June 2015 (Doc. ID 240195); published 21 July 2015

We describe the individual contributions to the intensity distribution of the parhelic circle for plate-oriented hexagonal crystals at exactly zero solar elevation using geometrical optics. An experimental as well as theoretical study of in-plane ray paths provides details on the mechanism for several halos, including the parhelia, the 120° and 90° parhelia, a blue edge, and the Liljequist parhelia. Azimuthal coordinates for associated characteristic features in the intensity distribution are compared with experimental data obtained using a spinning hexagonal glass prism.

OCIS codes: (010.1290) Atmospheric optics; (010.2940) Ice crystal phenomena; (010.1690) Color; (010.4030) Mirages and refraction.

http://dx.doi.org/10.1364/AO.54.006608

1. INTRODUCTION

Combined with a rotary stage, a single hexagonal rod can simulate the random orientations about the vertical axis in a large ensemble of plate-oriented crystals that cause halos such as parhelia (PH) [1]. This allows a detailed and instructive investigation of a series of phenomena using only ray optics supplemented by Fresnel's transmission and reflection coefficients. In particular, the parhelic circle (PHC), which is a circle at the solar almucantar that spans the entire azimuthal range of the sky [1–5], becomes apparent. Three different types of crystal populations can produce this halo, including plate-oriented, singly-oriented (horizontal columns) and Parry-oriented crystals. The former is typically the most common contributor. We therefore focus on plate-oriented crystals, experimentally and theoretically. The PH may be considered the most prominent contributor to the PHC intensity pattern. The 120° parhelia, the recently confirmed [6] blue spot, and the Liljequist parhelia, which appear at low sun elevations, are further features of the comparatively complex PHC. The ray paths that contribute to the PHC range from simple external reflection to more intricate paths involving two refractions and several internal reflections [1–3,5]. As we will show, prism experiments and ray-by-ray studies permit a rich understanding of several contributing mechanisms, at least for near-zero solar elevations.

The classic rotating prism experiment has been used ever since Bravais [2,7,8] employed equilateral triangular prisms in 1847 to study halos. Several more recent publications [9–13] reported on such single crystal laboratory demonstrations, showcasing their potential in understanding ice halo phenomena. In contrast with equilateral prisms, hexagonal glass prisms represent a fair analog of the hexagonal ice crystals, which usually produce halos. As homogenizing light pipes [14], high-precision glass prisms with a hexagonal cross-section have recently become commercially available (e.g., Edmund Optics GmbH). Artificial halos, which can be investigated, include several that cannot be produced with triangular prisms [10–13].

Although the index of refraction of the common BK7 glass prism material, $n = 1.530$ for blue light and $n = 1.515$ for red light, is different from that of ice of about $n = 1.31$, the dispersion is similar. Longer wavelengths (i.e., red colors) experience a slightly lower index of refraction than shorter wavelengths (blue colors). Consequentially, the coloring of the resulting halos is similar. Still, the angles at which they appear and the extent for each halo will differ. Effects due to birefringence of ice crystals [15,16] are also not expected to be reproducible with amorphous glass prisms, although with highly birefringent quartz prisms [17].

2. RAY OPTICS AND INTENSITIES

Using the laser beam of a focusable laser diode, the various types of ray paths that occur for a hexagonal prism can be investigated individually. Specifically, using a blue laser diode has the distinct advantage of a visible ray path throughout the prism via the excited autofluorescence of the prism material.

Some of the most important rays for the zero-elevation PHC (i.e., excluding rays entering the top face) are shown in Fig. 1. Discussion of these requires some classification. Here, adopt the system of the book by W. Tape [1]: A ray path is notated according to the order in which it encounters the prism faces. The top and bottom basal faces are numbered 1 and 2, respectively, while the remaining side faces are numbered 3 to 8 in counterclockwise fashion. Still, each ray will possess a mirror ray, but both will be named after the member, which gives rise to intensity toward the right side of the sun. A longer string corresponds to a more complex path.

Theoretical investigations of halo characteristics using geometrical optics [1,18–23] can be done using any of the freely available halo simulation tools. HaloSim [24], for instance,

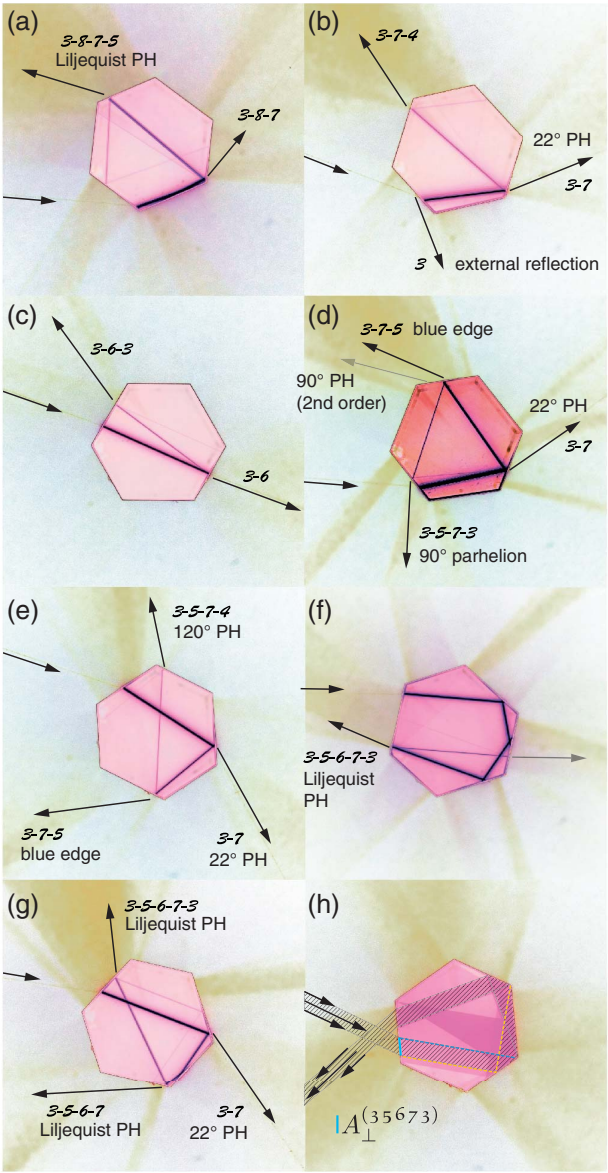

Fig. 1. (a)–(g) Color-inverted (false color) photographs of light rays through a BK7 hexagon using a focusable laser-diode. The exterior was exposure enhanced to reveal the free-space incidence beam. (h) Defocused parallel illumination shows a bundle of rays, each following the same path, determining the effective area $A_{\perp}$.

allows the refractive index to be set, and choosing a user-defined fish-eye perspective centering on the zenith allows simulation of the entire sky, including the full PHC. Details on polarization and additional diffraction [25] for small crystals may also be included in such models. Most importantly, these approaches allow nonzero solar elevations and different crystal orientations. However, while such software packages give a good impression of the whole sky and a wealth of information on the observable halos, the Monte Carlo approach employed does not lend itself to analytical progress concerning the angular positions of halo features.

A simpler and more insightful approach is suitable for the PHC due to plate-oriented crystals at zero solar elevations and our experimental conditions. Explicitly, we do not consider ray paths entering through the top face 1, such that the natural PHC's major contributors, 1–3–2 and 1–3–8–2, are not included. A detailed analysis of some in-plane ray paths and their geometrical constraints was outlined in [26–28]. By simply extending this approach to all major ray paths of the PHC, analytical expressions can be found for those azimuthal angles at which characteristic intensity features within the PHC appear, and the range of certain contributions can be given explicitly. The by-hand method further permits more insight to be gained about the factors that determine the intensity pattern. First, partial transmittance and reflection occur at the interfaces according to the squared Fresnel amplitude ratios r (polarization averaged). Depending on the incidence angle for each face encountered, a ray may also experience total internal reflection whenever the critical angle $\alpha_{\mathrm{TIR}} = \arcsin(1/n)$ is exceeded. The laser-beam's paths through the glass prism shown in Figs. 1(a) to 1(g) makes both phenomena directly visible: Two consecutive segments of the laser ray, i.e., before and after hitting a side face, will either show different or equal intensities depending on the particular incidence angle [see Figs. 1(f) versus 1(g)]. Second, geometrical constrains limit the effective area $A_{\perp}$ intercepted by the hexagonal crystal's side faces, typically being less than the full face of length L (times a unit height). Each path allows only a certain pencil of rays to emerge from the exit face [1], as exemplarily illustrated in Fig. 1(h). This effective area can be found by geometrical means as illustrated for a Liljequist PH ray path in Fig. 2.

The intensity $I(\theta)$ due to all m considered ray paths (each involving at most k internal reflections) can be found by binning the total deflection angles $\psi(m)(\delta)$ for all paths and distinct prism orientations $\delta \in [0, \pi/6]$ [28]. Each orientation and path then adds to the intensity, an amount,

$$dI(\theta) \propto \frac{A_{\perp}^{(m)}(\delta)}{2L} \prod_{i=1}^{k} r_{i(m)}^{2}(\delta), \tag{1}$$

multiplied with the appropriate transmittance through the entrance and exit faces (i.e., two factors of the form $[1 - r^2]$) and a projecting factor $\cos(\phi)$ multiplying $A_{\perp}$. Deflection angles lying within the left and right hemispheres are taken to contribute to the same intensity within $\theta(\psi^{(m)}) \in [0, \pi]$. Therefore, the pattern already repeats for prism-orientations δ exceeding $\pi/6$. Accordingly, only three faces need to be considered as possible entry faces [28]. For instance, the intensity distribution of the type 3–7 rays was computed via rays

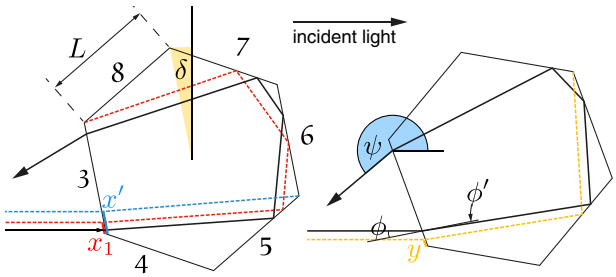

Fig. 2. Geometrical optics calculation: δ is the prism angle, $\psi = \pi + 2\delta$ the total deflection angle [13], ϕ the incident angle, and ϕ' the refracted internal angle, both related by $\sin(\phi) = n\sin(\phi')$. The sketched ray (black) is one of two possible 3–5–6–7–3 paths for $\delta \in [0, \pi/6]$. Its limiting ray paths (dashed) determine the lengths $x_1 = [-1 + 5\sqrt{3}\tan(\phi')]L/2$, $x' = \sqrt{3}\tan(\phi')L$, and $y = [-1 + 3\sqrt{3}\tan(\phi')]L/2$. y and x were obtained by successive application of the law of sines. For this entry face, the incidence angle is $\phi = \delta$. The effective area is then $A_{\perp}^{(3567)} = [\max(0, \min(x_1, x')) - \max(0, y)]$.

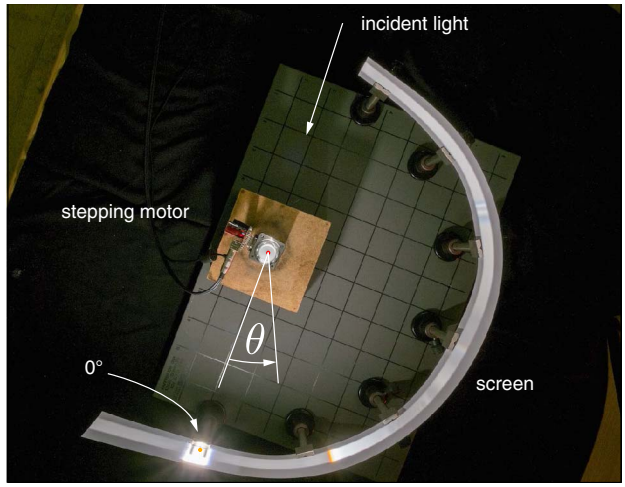

Fig. 3. Setup photographed from above for a rotating prism illuminated perpendicularly to the rod's long (rotation) axis. A tripod-mounted camera was used to take raw images from this perspective. Figures 4(b) and 5(b) show the spectra along the screen converted to an angular scale.

entering the three left-most faces in Fig. 2 (faces 3, 4, 8). The Visualization 1 gives a map containing >40 considered paths and their deflection angles as a function of the prism orientation, the limiting ray paths (geometrical constraints) determining the effective areas as well as the internal angles required to find the Fresnel coefficients. This map also annotates the specific paths that were used to arrive at the azimuth positions given throughout the article, using straightforward ray-optics only [13]. A corresponding open-source real-time implementation is available online.

3. ILLUMINATING A ROTATING PRISM

For a quantitative investigation and comparison with the theory, one may use any camera capable of taking RAW images and long exposure times. To reduce noise, the ISO setting should be set to its native setting. In our experiment, we have used a Fujifilm X-E1 camera with the XF 18–55 mm kit zoom lens, using a maximum exposure time of 30 s. The RAW files were then converted to linear TIFF images using the free software, MakeTiff [29]. This allows a quantitative assessment of the true intensity recorded by the camera. JPG files already involve a nonlinear processing done by the camera software and are, thus, only suitable for color images and the analysis of the perception of halo colorings. Using a camera tripod and rotating the prism using a stepper motor, average intensity patterns can be projected on a screen surrounding the prism, as shown in Fig. 3. The screen was not perfectly hemispherical, such that we used a polygonal path to extract the intensities along with the angular coordinates relative to the forward direction. To compare the experiment with theory, we first investigated the pattern using a monochromatic blue laser diode operating at wavelength of $\lambda = 405$ nm. Color images using a projector lamp were recorded next. We also translated wavelength-dependent theoretical intensity distributions into the color images using the spectrum of the light source, the CIE standard calorimetric observer response function, and a typical RGB conversion matrix of the tristimulus values [30]. For more realistic images, the nonlinear RGB values were computed and are shown for comparison along with the experimental data in Figs. 4 and 5. A similar procedure has previously been applied to study the visibility of tertiary rainbows [31].

Discussing the angular characteristics, we will use degrees when referring to specific angles and features while we will use radians in analytical expressions and relations between angles.

4. INDIVIDUAL CONSTITUENTS OF THE PHC

In the following sections, we discuss the most prominent features in the intensity distribution. The characteristic azimuthal angles will be given for BK7 glass and blue light ($n = 1.53$) and for ice prisms ($n = 1.31$).

A. 22° Parhelia

According to the ray classification, the ray paths responsible for the parhelia are labeled 3–7 [see Figs. 1(b), 1(d), and 1(e)]. It is well known that the halo angle corresponds to the angle of minimum deviation through an equilateral $\gamma = \pi/3$ prism [2,32]:

$$\sin\left(\frac{\theta_{\mathrm{PH}}^{\min} + \gamma}{2}\right) = n\sin\left(\frac{\gamma}{2}\right). \tag{2}$$

While for the ice halo the result is $\theta_{\mathrm{PH}}^{\min} \approx 22°$, for the BK7 glass prism, the angle becomes $\theta_{\mathrm{PH}}^{\min} \approx 38°$ [see Fig. 4(a)]. Red colors are refracted less; hence, the PH appears reddish toward the light source [see Fig. 4(b)]. The width of the PH can be found width the help of the angle of maximum deviation for grazing incidence on a prism [2], $\theta_{\mathrm{PH}}^{\max} = \pi/2 - \gamma + \arcsin(n\sin(\gamma - \arcsin(n^{-1})))$. The perceived width is more narrow than $\theta_{\mathrm{PH}}^{\max} - \theta_{\mathrm{PH}}^{\min}$ because the intensity near the fake caustic decays steeply as $(\theta - \theta_{\mathrm{PH}}^{\min})^{-1/2}$. The angular width of the sun of 0.5° broadens this divergence to a finite peak of about the same width [32]. This effect is also responsible for the characteristic concave–convex shape of the PH contribution near its peak in the intensity distribution [12,26,32],

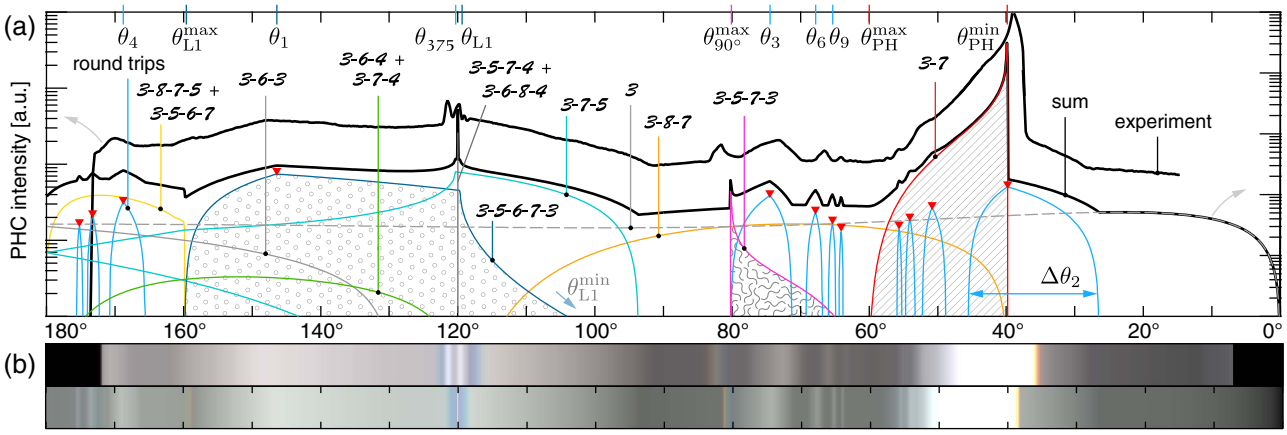

Fig. 4. (a) Azimuthal intensity distribution for parallel light incident on the glass hexagon (artificial PHC). Only the paths indicated were considered in the geometrical optics calculation, Eq. (1). Individual ray path contributions (colored thin lines) and their total sum (lower thick black line) are shown, along with the experimental data (upper thick black line). The triangles mark the round-trip ray path azimuths and intensities as computed with Eq. (8), Section 4.G. Some contributions have been textured to allow easier identification in Figs. 6 and 5. The data intensity scale (left) spans one decade less than the theoretical scale (right). (b) Experimental image (top) along the screen (see Fig. 3) and computed image (bottom). White areas correspond to overexposure/saturation.

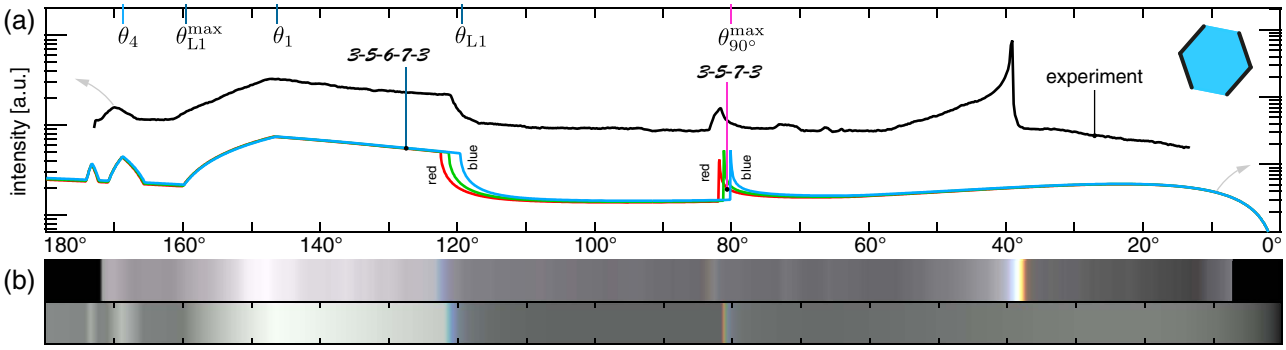

Fig. 5. (a) Total azimuthal intensity distribution when all but two opposing faces of the prism are masked (see inset sketch). The experimental data (black) as well as the geometrical optics calculation for $n = \{1.53, 1.52, 1.51\}$ (blue, green, red). The residual PH around 39° is due to imperfect masking. (b) Experimental image (top) along the screen (see Fig. 3) and computed image (bottom) for the cardboard-covered prism.

which we also observe in our experiment due to a similar divergence of the light source. The chromatic dispersion of the zero-elevation PH is about 1.1° for ice and 1.6° for BK7 glass, respectively.

B. External and Internal Reflections

The simplest tentative explanation of the parhelic circle is that it is caused by external reflections from the side faces of the hexagonal prisms [2] (i.e., the most simple rays categorized as 3), according to the only face they encounter [see Fig. 1(b)]. An analytical expression for the PHC intensity distribution based from this mechanism can be found in [4]. For natural ice halos, earlier studies already showed that external reflections contribute negligibly to the PHC [1]. Instead, the path 1–3–2 is by far the most common contributor at nonzero solar elevation. Even at zero solar elevation, different paths such as 3–8–7 become the most prominent contributors [1]. Only the latter ones are within the scope of the simple model discussed here. A brief examination of the experimental as well as calculated data leads to the conclusion that only within the near-forward direction between the light source and the PH grazing external reflections contribute appreciably to the total intensity [see the gray dashed versus the thick black line in Fig. 4(a)].

C. 90° Parhelia

In laboratory experiments, the so-called 90° parhelia were observed and explained [2,10] by the ray path 3–5–7–3 [see Fig. 1(d)]. Already the ray path suggests its close similarity to the ordinary 22° parhelia. The consecutive internal reflections by two faces making an angle $\gamma = \pi/3$ results in an additional deflection by $2(\pi - \gamma)$. Since the total deviation ψ exceeds 2π, the actual observed angle toward the light source will be $2\pi - \psi$. Accordingly, the analysis of the angle of deflection yields an angle of minimum deviation (but maximum angular distance from the light source) at $\theta_{90°}^{\max} = 2\pi/3 - \theta_{PH}^{\min} = 2\arccos(n/2)$, with an inverted color

sequence for this halo phenomenon, as compared with the common PH [see Fig. 4(b)]. Notably, the ray path is similar to the secondary rainbow, including the color sequence [33]. For ice, the halo would appear at about $\theta_{90°}^{\max} \approx 98°$, while for BK7 the angle is $\theta_{90°}^{\max} \approx 80°$. However, the fact that the intensity of the 90° PH is approximately 3 orders of magnitude fainter than the 22° PH adds to the explanation why it has not yet been observed in nature and makes future observation difficult at best. In the glass prism experiment, where the otherwise dominant path 1–3–2 is absent, the halo can be clearly observed. Following an approach originally due to Bravais [2], obstructing all but two opposing faces blocks out the intense 22° parhelia. Then, the 90° PH shows up as the brightest artificial full-spectrum halo [see Fig. 5]. It has been speculated before [2] that Hevel's curious halo from 1661 could be explained by this ray path, although full 3D ray-tracing simulations by W. Tape could not support this conjecture [1, Display 11-1]. Last, an even weaker second-order 90° PH has been observed by Bravais using a triangular prism [2]. Here, its ray path corresponds to 3–7–5–3–7–5, photographed and barely visible in Fig. 1(d), with a minimum deflection angle of $\theta_{90°,2}^{\min} = 2\pi/3 + \theta_{\mathrm{PH}}^{\min}$ and the same color sequence as the 22° PH. Its exceedingly faint PHC signature could not be observed.

D. 120° Parhelia

At zero solar elevation, the ray path 3–5–7–4 contributes to the 120° halo [1,2]. This path resembles the one responsible for the 90° PH, but, instead of exiting through the entry face 3, it exits through the adjacent face 4 [see Fig. 1(e)]. The internal angles for the entry and exit are identical such that no net refraction occurs [13]. Accordingly, one finds that such a ray experiences an orientation- and color-independent constant total deflection by $\psi = 4\pi/3$, corresponding to an eponymous azimuth of $\theta_{120°} = 2\pi - \psi = 2\pi/3$. The reverse path 3–6–8–4 is also possible. In the experiment, upon rotation of the prism, one observes a nonmoving bright spot. Although the deflection remains constant, a homogeneously illuminated prism will redirect a pencil of rays of different width and originating from different exit faces, depending on the orientation of the prism. If a screen is located far enough from the prism, this halo shrinks to the angular extent or divergence of the light source. This is similar to the natural counterpart, which has an extent determined by the angular width of the sun and the orientational ordering of the plate crystals. In the experiment, at closer distances the angular extent of this feature becomes limited by the size of the prism. Accordingly, two bright stripes in the experimentally recorded color spectra and two peaks in the monochromatic intensity appear [see Fig. 4(b)]. A further weaker contributor will be discussed in Section 4.G, accounting for the third weak peak seen best in the monochromatic spectrum.

E. Liljequist Parhelia

First observed by G. H. Liljequist in 1951 in Antarctica [34], the Liljequist parhelion denotes a low-elevation PHC intensity feature associated with rays that are totally internally reflected twice. It was first simulated by Tränkle and Greenler in 1986 [20] and then explained by Tape in 1994 [1]. It was subsequently investigated regarding its coloring with Monte Carlo methods by Moilanen in 1996 [35]. Unambiguous photographs of this rare halo can be found for Rovaniemi display (28 October 2012) and for the spotlight experiments done by Riikonen (Rovaniemi, 7/8 December 2008). Also in the book by Tape, the subparhelic counterpart is shown [1, Display 7-1]. For ice, this feature appears at about 27° to both sides of the anthelic point [see Fig. 6(b)]. Primarily, two ray paths contribute to this halo, namely, the 3–5–6–7–3 ray and the 3–8–7–5 (and its reverse 3–5–6–7) ray. Figure 1 shows photographs of both paths in (f) (g) and (a) (g), respectively. For BK7 glass, both paths cause PHC intensities at clearly separate azimuths. Considering the former ray path first, the angular extent and position are determined by two effects. A steep decrease in intensity occurs at an angle corresponding to the deflection angle of this ray when the identical internal reflections at interfaces 5 and 7 become total internal reflections, compared with the schematic in Fig. 2. The corresponding azimuth when this happens is given by [13]

$$\theta_{L1} = 2 \arccos\left(n \sin\left(\frac{\pi}{3} - \alpha_{\mathrm{TIR}}\right)\right). \tag{3}$$

For BK7 glass, the angle is $\theta_{L1} \approx 120°$. For ice, the azimuth is $\theta_{L1} \approx 153°$ and marks the coordinate of highest intensity of the Liljequist PH. For red light, the angle is larger by about 2° for ice and glass, such that the halo contains a transition from blue toward the sun over cyan to white [Fig. 6(c)]. This coloring is therefore not mediated by a net refraction of the rays that emerge from the prism, in contrast with the 22°- and 90°-PH. Experimentally, the effect is best seen when separated from other contributors in this "busy azimuthal domain" (Fig. 4 around 120°). Again, the obstruction of all but two opposing

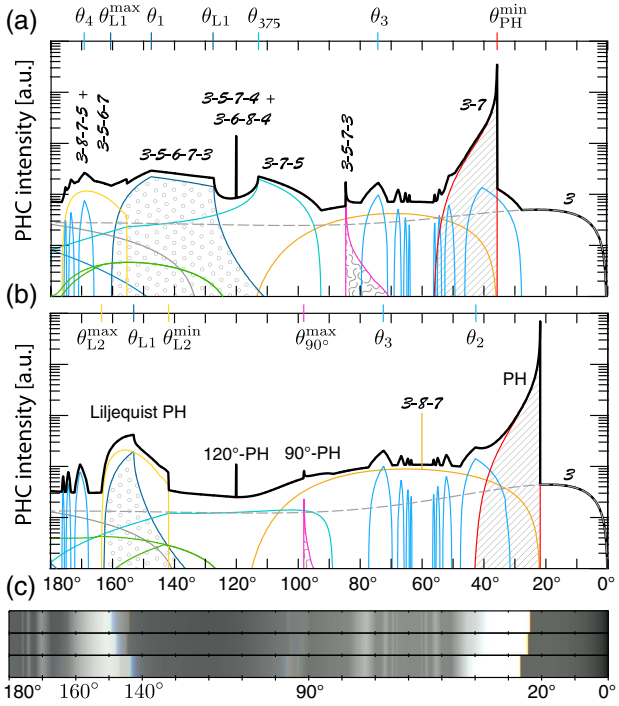

Fig. 6. Intensity plot as in Fig. 4(a) but for (a) acrylic glass, $n = 1.48$, and (b) ice, $n = 1.31$. (c) Coloring for ice material (PH are overexposed) at different light source elevations $e = \{0°, 10°, 20°\}$ (top to bottom).

crystal faces allows an individual investigation of this peculiar halo contribution (see Fig. 5). In particular, this restriction of partaking prism faces also eliminates the 120° PH and the overlapping 3–7–5 contribution. The maximum angle of this halo is determined by the geometrical constraint that the exit ray must still hit the entrance face ($x_1 > 0$, Fig. 2). Similarly, considering $y - x' > 0$ for the mirrored path entering through face 8, the minimum angle may be found. The azimuthal limits are then

$$[\theta_{L1}^{\min}, \theta_{L1}^{\max}] = \left[2 \arccos\left(\frac{n}{2}\right), 2 \arccos\left(\frac{n}{2\sqrt{19}}\right)\right], \quad (4)$$

such that the beginning of this feature coincides with the peak of the 90° PH (i.e., $\theta_{L1}^{\min} = \theta_{90°}^{\max}$). For ice, the azimuthal range is [98°, 163°], whereas for BK7 glass this amounts to a range of [80°, 160°] [see Fig. 4(a)]. The decay toward the low angle side at $\theta_{L1}^{\min}$ occurs about three decades below the plot range and is, thus, not seen in the figures.

The second contributor is the 3–8–7–5 ray path. Its azimuthal limits are found in a similar fashion from the geometry sketched in Fig. 7, specifically from $\psi_1(w = 0) \to \theta_{L2}^{\min}$ and $\psi_2(\delta = \pi/6) \to \theta_{L2}^{\max}$,

$$\theta_{L2}^{\max} = \frac{5\pi}{6} + \arcsin\left(n \sin\left(\frac{\pi}{3} - \alpha_{\mathrm{TIR}}\right)\right),$$
$$\theta_{L2}^{\min} = \frac{\pi}{3} + 2 \arcsin\left(\frac{n}{2}\right). \quad (5)$$

For BK7 glass, this corresponds to an azimuthal range of [160°, 180°], whereas for ice this corresponds to a range of [142°, 163°] [see Fig. 6(b)]. For ice crystals, both ray paths contribute almost equally to the Liljequist PH, while its visible angular width should be determined by the latter contribution (i.e., ∼21° at zero solar elevation). Figure 6(c) shows simulations of the coloring of artificial Liljequist parhelia at zero and small light source elevations and match the photographs from the spotlight experiments by Riikonen.

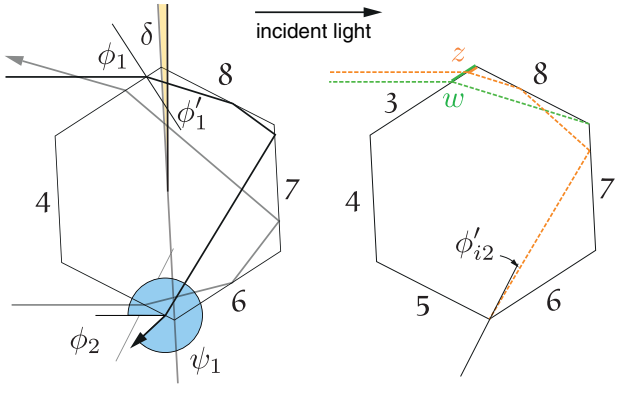

Fig. 7. Geometry and constraints leading to the azimuthal limits of the 3 – 8 – 7 – 5 contribution. The indicated lengths are $w = [-1 + \sqrt{3}\tan(\phi')]L/2$ and $z = [-2 + \sqrt{3}\tan(\phi')]L$, and the effective area is $A_\perp = \max(0, w) - \max(0, z)$. The incidence and deflection angles for the two possible rays are $\phi_1 = \pi/3 - \delta, \psi_1 = 2\pi/3 - \delta + \phi_{12}$ and $\phi_2 = \pi/3 + \delta$, $\psi_2 = 2\pi/3 + \delta + \phi_{22}$ with $\phi'_{i2} = \pi/3 - \phi'_i$ being the internal angles upon exit, and Snell's law applies $n \sin(\phi') = \sin(\phi)$.

F. Blue Edges

The blue spot phenomenon on the natural PHC was explained [6] by the properties of the ray path 1–3–2. A wavelength-dependent total internal reflection at interface 3 is responsible for the blue spot occurring at an azimuth $\theta_{132} = 2 \arcsin(n \cos(\arcsin(1/n))/\cos(e))$, with n being the material's index of refraction. Similarly, the ray path 3–5–6–7–3, encountered in the previous study of the Liljequist PH exhibits a blueish edge color at θ_{L1}. The same mechanism of wavelength-dependent total internal reflection causes the features observed in the experiment.

In the artificial PHC experiment, the contribution from the ray path 3–7–5, photographed in Figs. 1(d),1(e), also shows a blueish edge. This is due to the occurrence of total internal reflection at the second interface 7, leading to a steep drop-off of the intensity at a characteristic azimuthal angle θ_{375}:

$$\theta_{375} = \frac{\pi}{3} + 2 \arcsin\left(n \sin\left(\frac{\pi}{3} - \alpha_{\mathrm{TIR}}\right)\right) \quad (6)$$

(see Fig. 4). A derivation of this result was given in our recent reference [13]. The mechanism and internal angles coincide with those involved in the blue feature at θ_{L1}. Consequently, these two azimuths are related. Specifically, $\theta_{375} = 4\pi/3 - \theta_{L1}$. For BK7 glass, one finds $\theta_{375} \approx 120°$, shifting toward smaller angles for decreasing n {see Fig. 6(a) for acrylic glass with $n = 1.46$, as in [10]}. Since, accidentally, θ_{L1} and θ_{375} coincide for BK7 glass and occur at the position of the triplet 120° PH, a complex blue/white feature is seen in our experiment [see Fig. 4(b)]. For acrylic glass, these three features are more clearly apart [see Fig. 6(a)].

G. Round Trips

If the hexagon is oriented such that a face is almost normal to the incidence beam (δ small [see Fig. 2]), round trips can be observed for rays impinging on the face close to its end. The Liljequist PH ray path 3–5–6–7–3 constitutes the round trip of order $i = 1$. The construction of the i-th order round trip is now recursively defined as follows: The exiting face of the preceding round trip is replaced by two total internal reflections at the very same face and its predecessor, followed by exiting through the face opposite to the predecessor. Accordingly, the second-order $i = 2$ round trip ray path is 3–5–6–7–8–3–5. Figure 8 shows photographs of the first six round-trip rays, each increasingly deflected through $\psi_i = s\pi/3 + 2\delta$ with $s(i) = 2i + 1$. Each increase in the round-trip order adds 120° to the total deflection angle. The geometric constraints are $A_\perp^i = \max(0, \min(x', x_i)) - \max(0, x_{i-1}) > 0$ with x' of Fig. 2 and x_i of Fig. 8. Starting with $i = 2$, the azimuthal limits, determined by $x_{i-1} = x'$, $x_i = 0$, describe widths $\Delta\theta_i$ narrowing down as

$$\sin(\Delta\theta_i) \approx \frac{8n}{\sqrt{3}} s^{-2} + \frac{4n}{\sqrt{3}}\left[7 + \frac{n^2}{3}\right] s^{-4}, \quad (7)$$

which is accurate to within less than 1%. Starting with the first-order round trip, the maxima (peaks) occur when $x_{i-1} = 0$, i.e., for prism orientations $\delta_i = \arcsin(n/\sqrt{1 + 3\,s^2})$, and cause corresponding deviations (modulo 2π) of

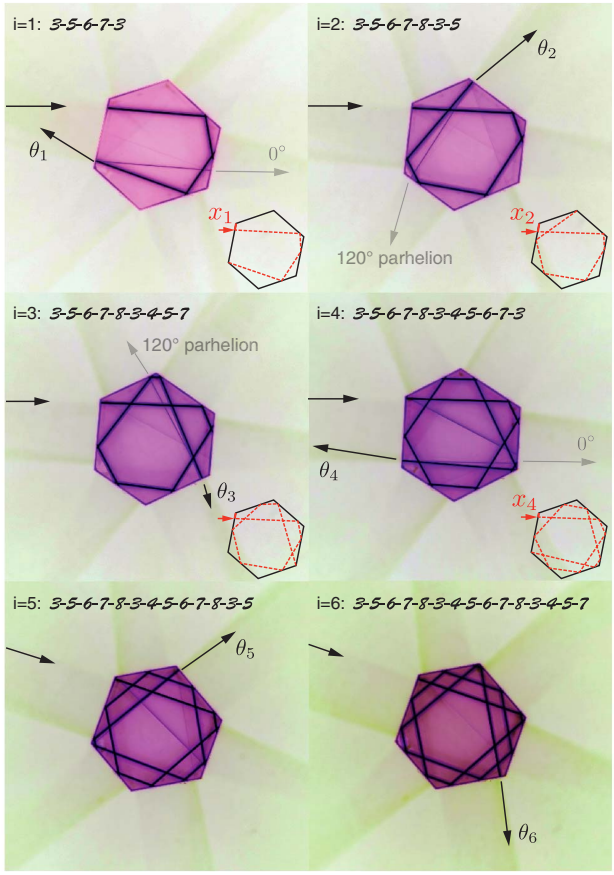

Fig. 8. Color-inverted (false color) photographs of round-trip light rays through a BK7 hexagon using a focusable laser diode. The insets show the limiting paths, similar to Fig. 2. The lengths are found to be $x_i = [-1 + (s+2)\sqrt{3}\tan(\phi')]L/2$, with $\phi = \delta$.

$$\theta_i' = \frac{\pi}{3}s + 2\arcsin\left(\frac{n}{\sqrt{1+3s^2}}\right) \bmod 2\pi, \tag{8}$$

such that they occur at azimuths of $\theta_i = \theta_i'$ or $2\pi - \theta_i'$ when $\theta_i' > \pi$. For BK7 glass and blue light ($n = 1.53$), these maxima occur at $\theta_{1,2,\ldots} = 146°, 40°, 74°, 169°, 51°, 68°, 173°, 54°, 65°$, and 175°. The sensitivity of the deviations in Eq. (8) on the refractive index is weak, such that these features appear colorless. Their intensity drops as $1/s$ such that most of them could be observed in the experiment [see Figs. 4(a) and 4(b)]. The reason for weak decay is that the total internal reflections occur at all but the entry and exit faces. The drop, thus, almost exclusively stems from the decreasing maximum $A_\perp^i$. The triangular solid markers in Fig. 4(a) show the angles computed with Eq. (8) and the scaling $\propto 1/s$.

A previous experiment also showed the first three round-trips [10], although they were not discussed and higher orders were absent, presumably due to the use of a lower-quality hexagonal prism. Recent ray-optics simulations that accompanied diffraction effect studies for ice prisms [25] exhibited the entire peak structure revealed in Fig. 6(b), although without discussing it. As this phenomenon requires near-perfect hexagons, it is doubtful whether any indication of the natural counterpart should be expected. If such ice halo should be observable,

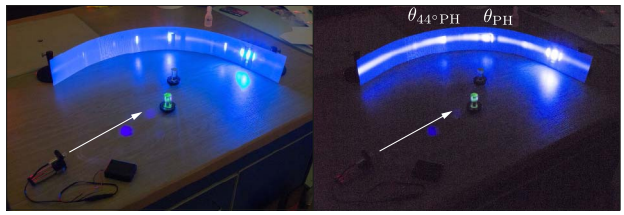

Fig. 9. Experimental setup for the demonstration of the mechanism causing the 44° parhelia. The left and right image shows the situation without and with rotation, respectively. The prisms have been mounted on axial ball bearings, which sustained rotation for a few seconds.

the features near $\theta_2 = 43°$, $\theta_3 = 72°$, and $\theta_4 = 170°$ for very low solar elevations are the best candidates [see Fig. 6(b)]. The appearance would indicate almost perfect hexagonal ice crystals. Riikonen identified a similar indicative ability [36]. He found that imperfect hexagons would result in the disappearance of the Liljequist PH. Finally, the partial retroreflection at the exit face of these rays (see Fig. 8) cause further faint contributions at azimuths of 120° and 0°, giving rise to the smallest peak in the experimental 120° PH triplet at finite screen distance [see Fig. 4(a)].

H. 44° Parhelia

Using two prisms, an artificial 44° parhelion [20] approximation may be produced. Placing a second prism close to the first prism at an angle corresponding to the PH angle θ_{PH}, the successive deflection through both prisms leads to a feature at twice the minimum deflection angle $\theta_{44°\mathrm{PH}}^{\min} = 2\theta_{\mathrm{PH}}^{\min}$ (i.e., the 44° parhelion). For BK7 glass, this halo appears at ≈80° and is clearly visible in the experiment (see Fig. 9). However, due to the closeness of the screen, especially in this setup, we did not quantitatively explore the azimuthal pattern.

5. OUTLOOK AND SUMMARY

In summary, we have presented a decomposition of the intensity distribution of a special artificial parhelic circle involving only in-plane rays. Based on a ray-by-ray analysis in geometrical optics, we gave explicit expressions for several characteristic angles on the PHC for plate-oriented crystals. Particularly, two superposing constituents of the Liljequist parhelia were shown to be connected to two corresponding but separable features in the glass-prism experiment.

Finally, we remark that the angular (azimuthal) positions of the discussed features for nonzero elevation $e \neq 0$ of the light source (or sun) relative to the basal prism faces can be accounted for using Bravais' index of refraction for inclined rays [2], as discussed in [13]. For the natural PHC, only at very low solar elevation are these features expected to be apparent above the background of the major contributing ray path 1–3–2. This shall be the subject of further inquiry.

Acknowledgment. We thank Axel Märcker for help with the experimental equipment from the lecture hall collection and thank the mechanical workshop of the Universität Leipzig. We thank Prof. Frank Cichos for financial support.

We also thank the anonymous referees who improved this manuscript with their comments.

REFERENCES

1. W. Tape, *Atmospheric Halos*, Antarctic Research Series (American Geophysical Union, 1994).
2. A. Bravais, "Mémoire sur les halos et les phénomènes optiques qui les accompagnent," J. de l' École Royale Polytechnique **31**, 1–270, §XXIV (1847).
3. W. Tape and J. Moilanen, *Atmospheric Halos and the Search for Angle x* (American Geophysical Union, 2006).
4. D. K. Lynch, "Polarization models of halo phenomena. i. the parhelic circle," J. Opt. Soc. Am. **69**, 1100–1103 (1979).
5. L. Cowley, "Atmospheric optics," http://www.atoptics.co.uk/halo/common.htm (2014).
6. M. Sillanpää, J. Moilanen, M. Riikonen, and M. Pekkola, "Blue spot on the parhelic circle," Appl. Opt. **40**, 5275–5279 (2001).
7. M. E. de Beaumont, *Memoir of auguste bravais* (Smithsonian Institution, 1869).
8. A. Wegner, "Die nebensonnen unter dem horizont," Meteorologische Zeitschrift **34-52**, 295–298 (1917).
9. M. V. Berry and S. Klein, "Diffraction near fake caustics," Eur. J. Phys. **18**, 303–306 (1997).
10. M. Vollmer and R. Tammer, "Laboratory experiments in atmospheric optics," Opt. Express **37**, 1557–1568 (1998).
11. M. Vollmer and R. Greenler, "Halo and mirage demonstrations in atmospheric optics," Appl. Opt. **42**, 394–398 (2003).
12. M. Großmann, K.-P. Moellmann, and M. Vollmer, "Artificially generated halos: rotating sample crystals around various axes," Appl. Opt. **54**, B97–B106 (2014).
13. M. Selmke, "Artificial halos," Am. J. Phys. **83**, to be published.
14. G. Zhu, X. Zhu, and C. Zhu, "Analytical approach of laser beam propagation in the hollow polygonal light pipe," Appl. Opt. **52**, 5619–5630 (2013).
15. G. P. Können and J. Tinbergen, "Polarimetry of a 22° halo," Appl. Opt. **30**, 3382–3400 (1991).
16. G. P. Können, S. H. Muller, and J. Tinbergen, "Halo polarization profiles and the interfacial angles of ice crystals," Appl. Opt. **33**, 4569–4579 (1994).
17. B. Fosbury, "Experiments with quartz hexagon," http://www.eso.org/~rfosbury/home/natural_colour/sky/halos/Quartz/quartz.html (1999).
18. R. F. Coleman and K.-N. Liou, "Light scattering by hexagonal ice crystals," J. Atmos. Sci. **38**, 1260–1271 (1981).
19. Y. Takano and K. Jayaweera, "Scattering phase matrix for hexagonal ice crystals computed from ray optics," Appl. Opt. **24**, 3254–3263 (1985).
20. E. Tränkle and R. G. Greenler, "Multiple-scattering effects in halo phenomena," J. Opt. Soc. Am. A **4**, 591–599 (1987).
21. Y. Takano and K.-N. Liou, "Solar radiative transfer in cirrus clouds. part i: single-scattering and optical properties of hexagonal ice crystals," J. Atmos. Sci. **46**, 3–19 (1989).
22. A. Macke, J. Mueller, and E. Raschke, "Single scattering properties of atmospheric ice crystals," J. Atmos. Sci. **53**, 2813–2825 (1996).
23. A. G. Borovoi, A. V. Burnashov, and A. Y. S. Cheng, "Light scattering by horizontally oriented ice crystal plates," J. Quant. Spectrosc. Radiat. Transfer **106**, 11–20 (2007).
24. L. Cowley and M. Schroeder, "HaloSim simulation program," http://www.atoptics.co.uk/halo/halfeat.htm.
25. P. J. Flatau and B. T. Draine, "Light scattering by hexagonal columns in the discrete dipole approximation," Opt. Express **22**, 21834–21846 (2014).
26. R. White, "Intensity plots of the parhelia," Q. J. R. Met. Soc. **103**, 169–175 (1977).
27. D. K. Lynch and P. Schwartz, "Origin of the anthelion," J. Opt. Soc. Am. **69**, 383–386 (1979).
28. M. Denny, "Calculation of the 22° halo," Eur. J. Phys. **18**, 432–435 (1997).
29. D. Dunthorn, C. Oldendorf, and C. F. Systems, http://www.colorneg.com/maketiff
30. R. J. Kubesh, "Computer display of chromaticity coordinates with the rainbow as an example," Am. J. Phys. **60**, 919–923 (1992).
31. R. L. Lee, Jr. and P. Laven, "Visibility of natural tertiary rainbows," Appl. Opt. **50**, F152–F161 (2011).
32. G. P. Können, "Polarization and intensity distributions of refraction halos," J. Opt. Soc. Am. **73**, 1629–1640 (1983).
33. J. D. Walker, "Multiple rainbows from single drops of water and other liquids," Am. J. Phys. **44**, 421–433 (1976).
34. G. H. Liljequist, *Halo-Phenomena and Ice-Crystals*, Vol. **2** of Norwegian-British-Swedish Antarctic Expedition 1949-52, (Norsk Polarinstitutt, 1956).
35. "Ursa minor 5/96," Sivuaurinko/Halot-Halos (1996).
36. M. Riikonen, "Liljequist parhelion does not exist," 2010,https://www.ursa.fi/blogi/ice-crystal-halos/liljequist_parhelion_does_not_exist/.